Journal of Power Sources 681 (2026) 240296

Contents lists available at ScienceDirect

Journal of Power Sources

journal homepage: www.elsevier.com/locate/jpowsour

Lithium-ion battery swelling characterisation using high-resolution optical fibre-based surface profiler and thermal imaging

Zhen Guo *, Md Abul Kashem, Calum Briggs, Lee Oldham, Anup Barai, James Marco

Warwick Manufacturing Group (WMG), University of Warwick, Coventry, CV4 7AL, United Kingdom

HIGHLIGHTS

- Distributed optical sensing captures surface and thermal profiles.
- Spatial data show bump-like swelling on charge and shrinkage on discharge start.
- Swelling causes—thermal, intercalation, rate—are classified, quantified.
- Rate dominates fast-charge swelling; anode deintercalation drives shrinkage.

ARTICLE INFO

Keywords:
Lithium-ion battery swelling
Distributed optical sensor
Surface profiler
Strain gradient

ABSTRACT

Although lithium-ion battery deformation is a fundamental issue in the battery industry, characterizing and optimizing battery swelling remains inherently difficult due to shortcomings in existing methods to assess multi-aspect swelling involving chemical, thermal, electrical and mechanical factors. This leads to substantial gaps in understanding the root causes of swelling in practical battery systems where individual cells are aggregated into complete packs. This paper proposes a novel distributed optical sensor with mm level resolution to reveal the complex underlying mechanism of battery swelling in multiparameter (current, voltage, temperature, strain) and multi-dimensional (surface profiler and thermal image) monitoring. Bump-like swelling profiles are found with the spatial-resolved optical measurement, indicating an easy strain accumulation in the central area of pouch cells. Different causes of battery swelling - thermal, lithium intercalation/deintercalation and applied current are systematically classified and validated. Fast charge/discharge induced swelling predominantly drives battery expansion. Lithium deintercalation happening on the anode primarily contributes to the cell shrinkage during certain discharge process (Depth of Discharge <20%). The contributions of each cause of battery swelling are systematically quantified, providing a deeper insight into swelling mechanisms and informing further optimization into cell operation and system integration.

1. Introduction

Lithium-ion battery (LIB) swelling is one of the essential issues for understanding battery performance, safety and capacity degradation throughout the entire lifespan of the cell [1]. With the urgent demand for the high gravimetric and volumetric energy density, especially in the electrical vehicles (EV) market, the issue of battery swelling is becoming more severe and unpredictable, particularly with the apparent industry direction towards silicon-based anodes [2,3]. The issue becomes critical within the confined space of battery packs and inherent lithium-ion battery swelling complicates the integration of cells into modules, packs, and battery systems. Essentially integrators must provide enough space around the cell for the unexpected swelling.

Despite significant research efforts from various perspectives, the underlying mechanisms of lithium-ion battery swelling remain unclear due to the complex interplay of electrochemical, thermal, and mechanical factors. Battery swelling studies can be summarized based on the view of scale: particle scale, components scale, and cell scale.

(a) At the particle scale, lithium-ion movement within active electrodes are the primary contributors to swelling. In graphite anode, lithium intercalates into the graphite structure, undergoing multiple phase transitions, such as the Li_xC_6 phases, as described in the phase diagram of Li_xC_6 [4–6]. This intercalation

* Corresponding author.
E-mail address: Zhen.Guo@warwick.ac.uk (Z. Guo).

https://doi.org/10.1016/j.jpowsour.2026.240296
Received 28 January 2026; Received in revised form 7 April 2026; Accepted 30 April 2026
0378-7753/© 2026 The Authors. Published by Elsevier B.V. This is an open access article under the CC BY license (http://creativecommons.org/licenses/by/4.0/).

process induces nonlinear deformation of the graphite lattice, exacerbated by concentrated lithium-ion gradients, which amplifies the complexity of swelling within the battery [7,8]. For silicon doped anodes, the swelling mechanism is more pronounced due to the large volumetric expansion that occurs during lithium intercalation/alloying. The significant plastic deformation of silicon particles, along with the potential for fracturing, leads to mechanical stresses that not only contributes to swelling but also accelerate battery degradation [9,10]. The repeated lithiation and de-lithiation cycles cause cumulative damage to the electrode structure, further intensifying capacity fade and reducing the overall lifespan of the battery [11,12].

(b) At the component scale, several factors contribute to the swelling of lithium-ion batteries. One of the keys is the formation of the solid electrolyte interface (SEI) on the anode during initial cycling. SEI formation induces irreversible volume changes, and higher degrees of SEI swelling are often correlated with poorer electrochemical cycling performance due to a loss of lithium inventory [13–15]. In addition to SEI formation, lithium plating and dendrite growth further exacerbate swelling. These phenomena not only result in capacity loss and impedance increase but also contribute to significant deformation of the battery structure [16–18]. Another important aspect of swelling is the internal gas generation, which depends on the specific composition of the electrodes and the electrolyte. Gas accumulation, primarily localized at the electrode/electrolyte interface, is typically irreversible, and its limited solubility in the electrolyte prevents it from being reabsorbed [19–21]. As the internal gas pressure increases, it can substantially alter the physical structure of the battery, especially in softer casing materials such as pouch cells.

(c) At the cell scale, swelling is influenced by the factors such as, jellyroll winding, the dimensions of the tabs, and casing materials. The swelling behaviour of lithium-ion batteries can be characterized through various methods, including measurements of cell deformation (such as displacement sensors [22,23], dilatometry [24], 3D cameras [25], and X-ray imaging [26,27]), swelling force [28], surface and internal strain [29,30], and internal pressure [31]. These techniques provide a comprehensive understanding of the mechanical changes that occur during battery operation. Multiple displacement measurements are investigated to correlate the prismatic cell case deformation to electrochemical transformation in individual anode/separator/cathode layers [23]. The gas pressure in the 21700 cell is obtained by internal instrumented sensor to deliver the nonlinear relationship between the gas pressure generation and battery state of charge [31].

Physical phenomena within the active materials associated with lithium intercalation/deintercalation provides the foundation for the battery deformation and various methodologies have been introduced to investigate the cell swelling behaviour. Each of these scales offers distinct insights into the swelling behaviour, but a comprehensive understanding of the phenomenon requires an integrated approach that considers the multi-scale interactions. Battery swelling is still far from fully understood, making the optimization of systems integration a practical challenge.

Following aspects required to be addressed for the further battery swelling investigation: firstly, a multi-parameter approach is essential, as battery swelling is influenced by various factors that must be studied in combination. For example, the temperature is not just crucial to the battery performance, it also affects the battery swelling by dominating lithium intercalation and diffusion [32], internal gas generation and expansion [33]. The thermal behaviour is also determined by applied C-rate [34,35]. This requires the expansion of sensor methodology to multi-parameter monitoring (i.e. concurrent measurement of current, voltage, temperature, strain, pressure, ion density et al.). Second, the swelling behaviour investigation should move beyond the point-sensor to spatially resolved characterisation with the increasing physical size of cells. This helps to facilitate scaling up monitoring from a single cell to the level of a module or pack. Finally, the in-situ, non-invasive and lower cost sensor instrumentation are preferable to comply with the requirements of current battery management system (BMS).

Optical fibre sensor is a promising method for advanced battery instrumentation due to the compact dimension (sub-mm) and nonconductive material (silica) [36,37]. Additionally, optical fibre sensors are multi-sensitive to both temperature and strain, which enables multiscale investigation [38,39]. In this paper, we propose an optical fibre-based surface profiler and thermal imaging for the battery swelling characterisation. Unlike the point-like fibre Bragg grating (FBG) and Fabry-Perot(F-P) based optical sensor, the proposed distributed optical fibre sensor offers ultimate mm-level resolution to spatially characterize the swelling and thermal behaviour of the entire cell. The measured surface strain in this study is intended to characterize the trend of cell swelling rather than to directly quantify swelling force or internal/stack pressure. Furthermore, this methodology systematically calibrates the relationship between swelling induced by various factors, including thermal effects, lithium intercalation, and applied C-rate. The systematic integration of these factors allows for a more holistic understanding of battery swelling behaviour and provides critical insights into the interactions between thermal, electrochemical, and mechanical processes that drive battery deformation.

2. Method and experiment setup

2.1. Distributed optical sensor based on optical frequency domain reflectometer

In an optical frequency domain reflectometer (OFDR), a wavelength-tuneable laser is launched into the fibre, as shown in Fig. 1(a). Elastic Rayleigh backscattering inevitably occurs along the fibre length during light transmission. The randomly distributed refractive index in the fibre creates a unique *fingerprint* to allow for precise location of induvial elements along the fibre. The frequency of reflected Rayleigh backscattering is thus linearly related to the position along the fibre length. While applied external temperature and/or strain affects the fibre refractive index at specific position, it will result in a shift in the Rayleigh backscattering spectrum (RBS), which can be calibrated to quantify the changes in temperature/strain. In the optical frequency domain reflectometer, the light from the tuneable laser source is [40]:

$$E(t) = E_0 \, exp\{j[2\pi f_0 t + \pi\gamma t^2 + e(t)]\} \tag{1}$$

where f_0 is the initial frequency and γ is the laser sweep rate. The reflected Rayleigh scattering from the fibre under test is collected and interfere with localise reference light. The generated optical frequency domain reflectometer signal is:

$$I_{OFDR}(t) = {E_1}^2 \, cos\left\{2\pi\left[f_0\tau + \gamma\tau t + \frac{1}{2}\gamma\tau^2 + \varphi_n(t,\tau)\right]\right\} \tag{2}$$

where τ is the time delay between the sensing position z and the reference arm of the interference. Thus, the item of $\gamma\tau t$ creates the relationship between the spatial location of τ_z with the specific frequency of $\gamma\tau_z$. The theoretical spatial resolution of the OFDR is determined by:

$$\Delta z = c/2n\upsilon_{sweep} \tag{3}$$

The Rayleigh backscattering spectrum is then calculated based on a series of spatial resolution. The designed resolution is 3 mm and the wavelength sweep range is 10 nm, therefore, it needs 37 points to form such spatial resolution for the slide-window and cross-corelation process.

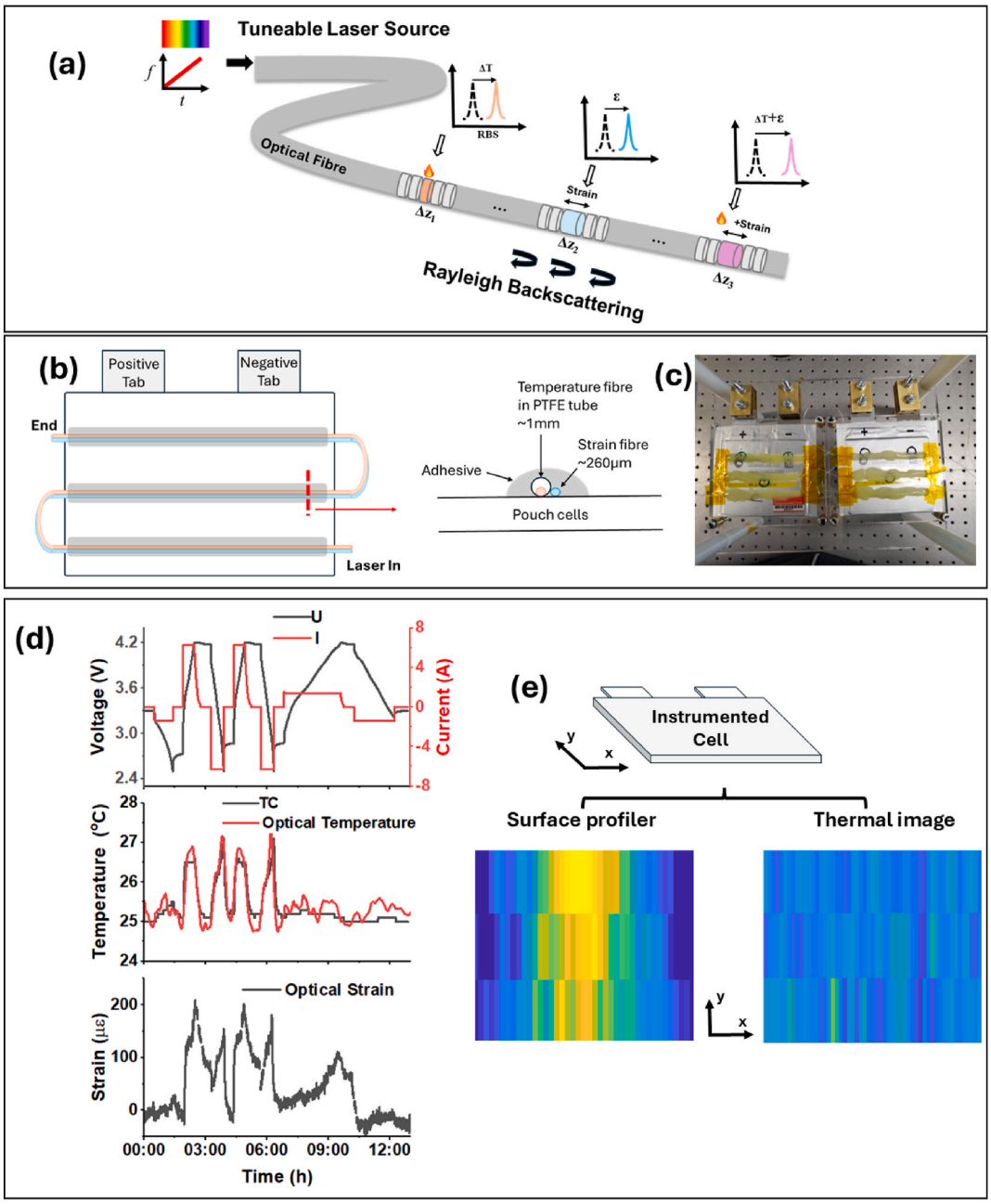

Fig. 1. Optical fibre-based battery surface profiler and thermal image. a. Schematic diagram of optical frequency domain reflectometer. b. Layout of the instrumented optical fibre on the pouch cells. c. Experimental set up of optical fibre instrumented pouch cells. d. The temperature and strain profile of the battery operation under 1.5C CC-CV charge and 1.5C CC discharge. e. Battery surface profiler and thermal image with 3 mm resolution at the time instance of end of CV charge.

The nonlinear laser sweep $\gamma(t)$ and phase $\varphi_n(t,\tau)$ in OFDR blur the theoretical resolution and deteriorates the distributed measurements. We proposed to employ an auxiliary interferometer and equal frequency resample to compensate for the nonlinear sweep noise. The instantaneous frequency value of $\upsilon(t)$ is modified by overall distribution of frequency sweeping [41]:

$$\upsilon(t) = \upsilon_{t-t_0} + \int_{t-t_0}^{t} \frac{1}{2\pi\tau}\frac{d\varphi(t)}{dt}dt \tag{4}$$

The OFDR experimental setup and demodulation are shown in Supplementary1- Fig.S1 and Fig.S2. Intrinsic noise sources in OFDR, such as nonlinear laser sweeping and laser phase noise, degrade the spatial resolution and accuracy of measurements. To address these challenges, an equal frequency resampling and wavelength calibration technique is implemented [41,42]. This method improves the spatial resolution, enabling the OFDR system to achieve a 3 mm resolution, which is critical for high-precision battery swelling characterisation.

2.2. Optical sensors calibration and instrumentation

Since the optical fibre is inherently sensitive to both temperature and strain, one single fibre is unable to differentiate between thermal-induced and strain-induced variations. To overcome this limitation, two optical fibres are used for this temperature-strain discrimination. The optical sensor instrumentation is shown in Fig. 1(b). One fibre function as a temperature sensor, while the other serves as a strain

sensor. The temperature sensor is designed to be strain-free by loosely inserting a bare fibre into a 1 mm diameter polytetrafluoroethylene (PTFE) tube, isolating from mechanical interference. This configuration allows the fibre to only sense temperature variation. Meanwhile, the strain sensor is a bare optical fibre exposed to both temperature and strain, allowing to capture combined effects. To isolate the pure strain measurement, the temperature-induced variation can be compensated by subtracting the temperature sensor's output from the strain sensor. Although the OFDR interrogator provides a nominal optical spatial resolution of 3 mm, the effective thermo-mechanical resolution of the present sensing configuration may be lower due to sensor packaging and bonding effects. The temperature fibre may exhibit some thermal lag relative to the pouch surface. Meanwhile, the bonded strain fibre may be affected by non-ideal strain transfer, adhesive compliance, and local mechanical averaging.

Three fibre segments are horizontally instrumented on the pouch cells surface in Fig. 1(c). Temperature and strain sensors are placed close to each other to minimize the thermal/strain difference. Both optical strain sensor and temperature sensor tube are tightly bonded to the pouch cell surface with adhesive, ensuring stable contact and reliable signal transmission during operation. OFDR frequency shift exhibits a linear relationship with the temperature variation, demonstrating a coefficient of correlation of 0.985. The sensitivity of optical measurement is 1.55 GHz/°C. OFDR frequency shift exhibits a linear relationship with the strain variation, demonstrating a coefficient of correlation of 0.998. The sensitivity of optical measurement is 0.13 GHz/με. Based on the optical fibre instrumentation, position calibration is conducted out by a heated metal cube to identify the fibre segment attached on the cell surface. To the strain optical sensor, the bottom segment starts from 865 mm and ends at 988 mm. The middle segment starts from 1120 mm and ends at 1243 mm. The top segment starts from 1495 mm and ends at 1621 mm. The corresponding thermocouple location is 1181 mm along the fibre length. The data processing of middle segment should be careful. Because it has a reverse instrumentation (left to right) compared to the bottom and top segment (right to left).

The spatial resolution for the temperature and strain measurement is 3 mm. The sampling rate is 1Hz. A BioLogic VSP 300 is used to control and monitor cell operation. The reference thermocouple is from RS PRO Type K. Thermocouple data is recorded via a Pico Logger. The sampling rate is 1Hz. The instrumented cell is located within the thermal chamber (Binder MKF56) to maintain ambient temperature. The pouch cell works between 2.5V and 4.2V and capacity is 4.2Ah. Cell charge and discharge follow a conventional constant current - constant voltage (CC-CV) charge and constant current (CC) discharge protocol. During charge, the cell is charged to the maximum voltage of 4.2V, at which point the voltage is held at the upper limit until the value of current is reduced to C/20. For discharge, a constant current rate is applied to reduce the voltage to the lower limit of 2.5V.

3. Result

3.1. Surface profiler and thermal image of lithium-ion pouch cell

Under a 1.5C constant current - constant voltage (CC-CV) charge and CC discharge profile, the constant current is 6.3A and the CV stops while the current reaches to C/20-0.21A. The temperature and strain behaviour in time domain is illustrated in Fig. 1(d). Optical measurement is obtained from the location of the surface centre. A thermal couple is placed at the same position for calibration and validation. The peak temperature is 26.5°C during the charge and 27.1°C during the discharge, indicating that the discharge process produces more heat than the charge. This result is consistent with that presented in Ref. [43]. Conversely, there are more strain generations during the charge process compared to the discharge. The strain peak at the charge process is 201.1με, while the discharge strain peak is around 166.3με, mainly caused by the lithium-ion intercalation into anodes.

The spatially resolved optical measurement, presented in Supplementary1-Fig. S4, reveals three distinct peaks, each corresponding to an instrumented optical fibre segment attached to the cell surface. The observed strain gradients clearly indicate that the cell undergoes non-uniform swelling during operation. Furthermore, the extracted swelling profile exhibits a characteristic deformation pattern, offering new insight into the underlying mechanical evolution of lithium-ion cells and their internal structural dynamics under electrochemical cycling.

After optical fibre position calibration, high-resolution surface profiling and thermal imaging are presented in Fig. 1(e). The surface profiler can be calculated from measured strain as depicted in Supplementary1-Fig. S7. The time instance of Fig. 1(e) is selected from the rest period after the CV charge. It is found that the strain is not evenly distributed after cells are fully charged. Residual strain is more easily accumulated and concentrated in the central area. This finding underscores the localized nature of strain accumulation on the soft pouch cells surface. In contrast, the thermal imaging reveals no significant thermal gradient across the cell's surface during this period, indicating that heat dissipation may not be a major contributing factor to strain accumulation in this instance.

3.2. Battery swelling characterisation with distributed optical sensor

The battery swelling process now can be investigated under multiple scales (strain and temperature) and multiple dimensions (time-spatial) based on the proposed methodology. The evolution of surface profiling and thermal imaging provides detailed insights into battery behaviour, as illustrated in Fig. 2. The CC charge process (A→B) undergoes a temperature increase due to the exothermic reaction inside the battery, while the battery surface also expands in an approximately uniform pattern. The maximum strain reaches 232.1με at point B. With the decreasing current in the CV charge (B→C), the cell temperature reduces to ambient due to excess thermal dissipation. Of particular interest is that the battery starts to shrink with the gradually decreasing current during the CV phase. This is counter intuitive, because the lithium intercalation still occurs with the applied current [4–6]. This indicates that battery swelling is influenced by multiple parameters, such as temperature, lithium-ion intercalation/deintercalation, and the current–voltage characteristics of the cell. At the end of CV charge, the measured strain at the surface central is around 101.2με, only 43.6% of the value at CC charge peak.

It has been mentioned, at point C, the strain is not uniformly distributed along the horizontal surface; instead, it forms a bump-like profile, with strain accumulation predominantly concentrated at the centre. At this stage, the temperature returns to ambient, and no current is applied. The causes of thermal-induced and fast charge-induced swelling effects diminish [44,45], thus lithium intercalation should be main cause for such surface strain profile.

At the beginning of CC discharge, the battery continues to shrink (C→D). During this stage, the temperature has not yet started to rise, indicating that the primary cause of battery deformation is lithium deintercalation. With the CC discharge progressing (D→E), increased heat generation becomes the dominant factor to drive battery swelling, mirroring the behaviour observed during stage B. Therefore, under a high-rate charge/discharge, the fast exothermic reaction easily contributes to the battery swelling.

The thermal images indicate that the surface thermal distribution across the battery is largely uniform (Fig. 2 bottom). In contrast, the strain distribution on the surface is not uniform. At Stage C, for example, the strain difference between the centre and edge regions exceeds 100με, highlighting significant spatial variation in mechanical deformation. Furthermore, during stages B and E, where substantial strain generation occurs, the strain distribution profiles are not identical. This variation underscores the necessity for a spatial-scale investigation to fully understand the complex behaviour of strain within the battery and the

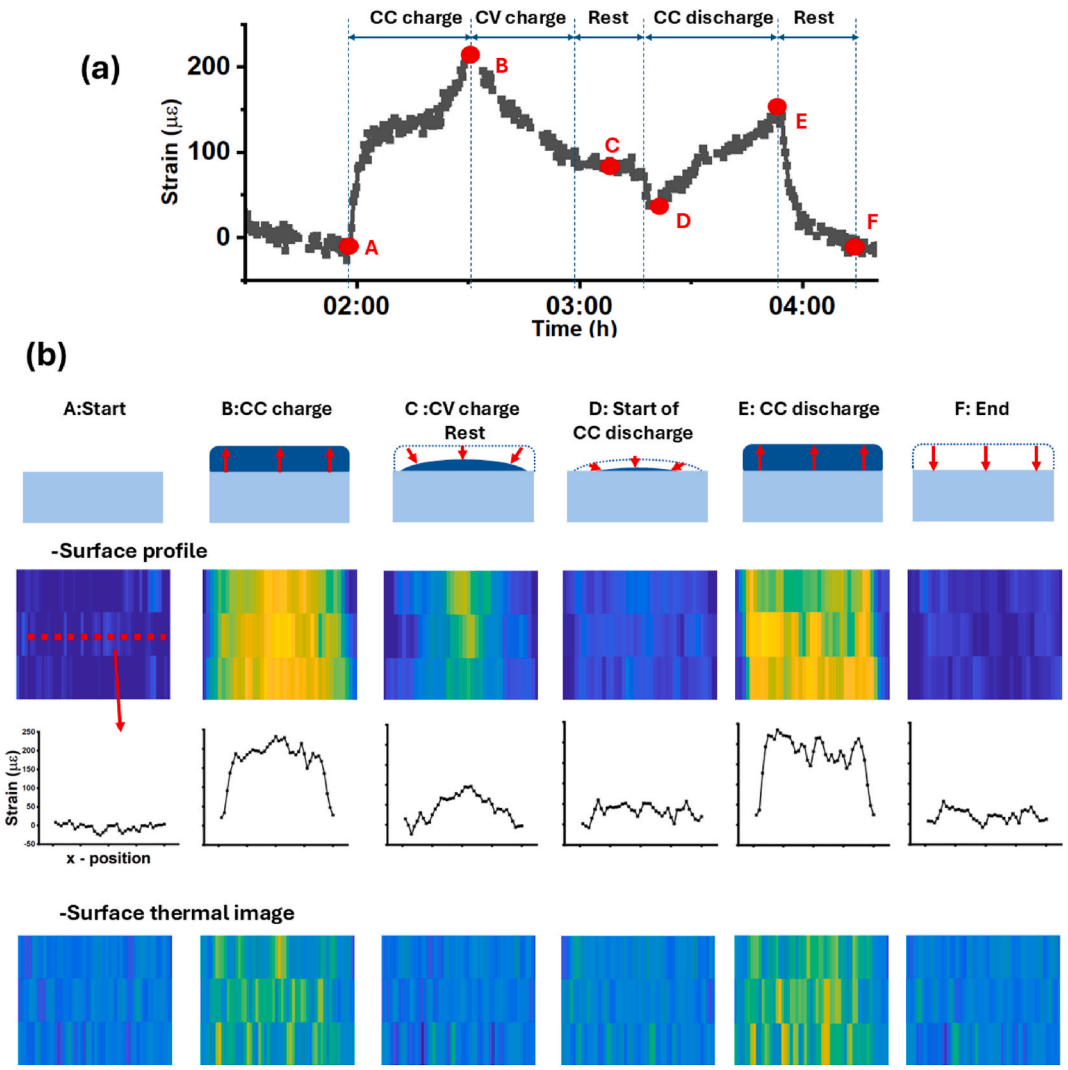

Fig. 2. Battery sweeling profile under a 1.5C CC-CV charge and 1.5C CC discharge. a. Strain profile in time-domain. The data is collected from the centre position of pouch cell surface, corresponding to the fibre position of 1181 mm. b. Battery surface swelling profile and thermal image under specific time instance. The lines are derived from the centre segment of instrumented optical fibre.

potential for strain induced failure modes.

Thermal generation, lithium intercalation and applied C-rate are the main causes of the battery swelling. But it is a complex system to be understood by involving all factors. It is noted that the definition of C-rate induced swelling is not limited to applied current/voltage. It includes all the left factors, such as internal gas generation, packaging constrains and other coupled mechanical factors. Generated heat from electrochemical reactions leads to material expansion and significantly influences the electrochemical processes, including lithium diffusion and electrical resistance within the cell. As discussed within [46,47] this thermal generation and gas volume not only contribute directly to the physical deformation of the battery but also alters the kinetics of the electrochemical reactions taking place. Additionally, the swelling induced by lithium intercalation is influenced by both the applied temperature and the C-rate. The C-rate dictates the rate of lithium intercalation, which in turn governs the phase transitions within the material [44,48]. These phase transitions are critical for understanding how lithium ions move into and out of the electrode materials, and they contribute to the overall thermal generation.

Aided by the proposed optical sensor with multi-parameters and multi-dimensional monitoring capabilities, we define the following to discriminate and decouple the root causes of battery swelling for a quantifiable investigation:

a. Thermal induced battery mechanical swelling - defined as battery mechanical expansion purely caused by temperature variation, without considering of subsequent thermal effect on the battery internal electrical and chemical reaction.
b. Lithium intercalation/deintercalation induced swelling - defined as an ideal lithium movement into and out of cathode and anode, without considering thermal generation and lithium diffusion affected by applied C-rates.

To investigate the defined mechanisms of thermal-induced swelling and lithium intercalation/deintercalation-induced swelling, the following experiments are designed:

a Thermal induced battery mechanical swelling

The authors designed a battery temperature cycle experiment without any electric load. Thermal effects are mitigated under the present experimental conditions, although a residual thermal contribution cannot be completely excluded. Designed temperature cycle profile is 10°C-50°C-10°C at steps of 5°C. The duration of each temperature is 2 h. Self-charge/discharge is not considered here due to short-term experiments. The SoC of the battery is maintained at 30%. The point-like strain measurement is selected from the centre of battery surface.

The instrumented optical fibre successfully detects strain generated by pouch cell expansion and measures the applied temperature simultaneously. The temperature sensor, positioned within the PTFE tube, serves to compensate for cross-sensitivity between temperature and strain measurements. The temperature induced frequency shift (blue line in Fig. 3 (a)) increases from −143.2 GHz at 10°C to 244.9 GHz at 50°C. The compensated strain is −697.0 GHz at 10°C and 867.1 GHz at 50°C (red line in Fig. 3(a)). Therefore, the sensitivity of temperature and thermal induced strain is 29.7με/°C. The R-square (coefficient of determination), representing the sensitivity is 0.998, indicating a good linear relationship between temperature changes and the measured strain.

When compared to the swelling value of 101.2με observed at Stage C, it is noteworthy that a one-degree temperature variation corresponds to approximately 29.3% of the total strain generated at full state of charge, indicating the significant influence of temperature variations on mechanical expansion in lithium-ion batteries.

Although the thermo-mechanical response of the pouch cell may depend on SoC, stress state, and electrochemical history, these effects are assumed to be of secondary importance within the limited operating window considered in this study. Therefore, the thermal strain sensitivity coefficient used here should be regarded as an effective coefficient for the tested conditions rather than a universal constant.

b Lithium intercalation/deintercalation induced swelling

The authors designed an experiment in which the battery is operated at a low C-rate to investigate the lithium intercalation-induced swelling. The low C-rate aims to minimize thermal generation and simulate the ideal lithium intercalation/deintercalation. The SoC gradually changes at the step of 10%. The C-rate employed is C/10. Each step is followed by 30-min rest. Results highlight that the temperature variation is limited to within ±0.5 °C in Fig. 4(a)-middle, efficiently minimising the thermal induced mechanical swelling. However, other coupled factors, including concentration gradients, viscoelastic relaxation, mechanical redistribution, and residual thermal effects, may still contribute to the measured response. Therefore, the results are interpreted as an approximation of intercalation-dominated swelling, rather than a strict isolation of swelling caused solely by lithium intercalation.

The strain gradually increases during the charge process. The maximum strain value under 100% SoC reaches 102.8 με in Fig. 4(a)-bottom. We should note that this is the same value of Stage C in Fig. 2 (after CV-charge). The spatial resolved optical measurement is shown in Supplementary1-Fig. S6. The surface profiler at 100% SoC presents the identical bump-like pattern as the Stage C in Fig. 4(b). This observation reinforces the conclusion that lithium intercalation-induced swelling is more pronounced at the centre of the pouch cell, indicating that for this cell, there is a tendency for swelling to accumulate in this region.

During cell discharge, the strain significantly decreases while the battery starts discharging from 0% to 20% depth of discharge (DoD). The measured strain drops from 84.7με to −4.5με. Such significant reduction in strain corroborates the findings from Stage D in Fig. 2, confirming the occurrence of battery shrinkage/compression during this phase. With the further discharge to 50% DoD, the strain slightly increases to 6.5με and then stays around zero for the remaining discharge process. This behaviour indicates that, at low DoD (<20%), the contraction is associated with lithium deintercalation from the anode; however, the relaxation of mechanical stresses accumulated during the charging process may also contribute to the measured deformation. With the present experimental approach, the purely chemical and mechanical contributions cannot be independently resolved.

Both the voltage and strain exhibit a ‘relaxation’ after each step of charge/discharge in Fig. 4(c). The voltage relaxation observed is attributed to the overvoltage conditions experienced by the electrodes under applied current. This is a common occurrence in lithium-ion batteries. The overvoltage can lead to temporary imbalances in the electrochemical potential, resulting in a subsequent relaxation as the system stabilizes. Similarly, strain relaxation may indicate the over-intercalation or deintercalation of lithium within the battery. When the applied charge current is halted, concentrated lithium ions at the interface between the electrodes and electrolyte may redistribute. Such relaxation is also found during the battery internal pressure investigation [31].

The red dots in Fig. 4(d) represent the strain values immediately after the respective charge/discharge phases, while the black dots indicate the strain measurements after a 0.5-h rest period. During the charge process, a characteristic 'swell-shrink' profile is observed, reflecting the expected behaviour of the battery as lithium intercalates into the anode/movement from the cathode. In contrast, during the initial discharge phase (<20% DoD), the strain profile exhibits a reverse trend—'shrink-swell.' This behaviour can be attributed to significant lithium deintercalation occurring during this stage, leading to a rapid reduction in strain as the anode releases lithium. With the discharge progressing, the profile returns to the normal model of ‘swell-shrink’. The strain behaviour during the high DoD (>30%) is stable (Fig. 4(d)-right). There are repeatable about 10 με strain generating and disappearing along the ‘swell-shrink’ profile. If the 10 με-strain at the high DoD (>30%) discharge is caused by the generated heat, the required temperature variation would be 0.3°C based on the derived sensitivity. As the 0.3°C is beyond the current accuracy of temperature sensor. This assumption can be further validated by the high accurate temperature sensor.

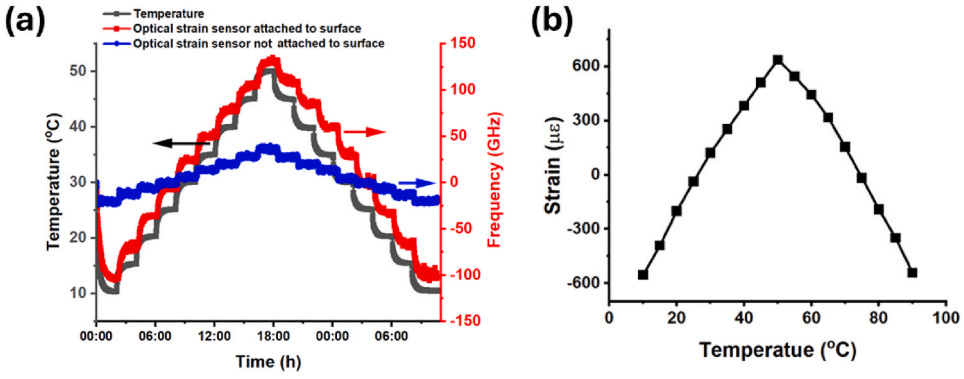

Fig. 3. Thermal-induced battery swelling calibration. a. Temperature cycle profile of 10°C-50°C-10°C (black curve), optical measurement under the influence of temperature and strain (red curve), optical measurement under the influence of temperature (blue curve). b derived sensitivity between the applied temperature and thermal induced strain, after the compensation of temperature cross-sensitivity. (For interpretation of the references to colour in this figure legend, the reader is referred to the Web version of this article.)

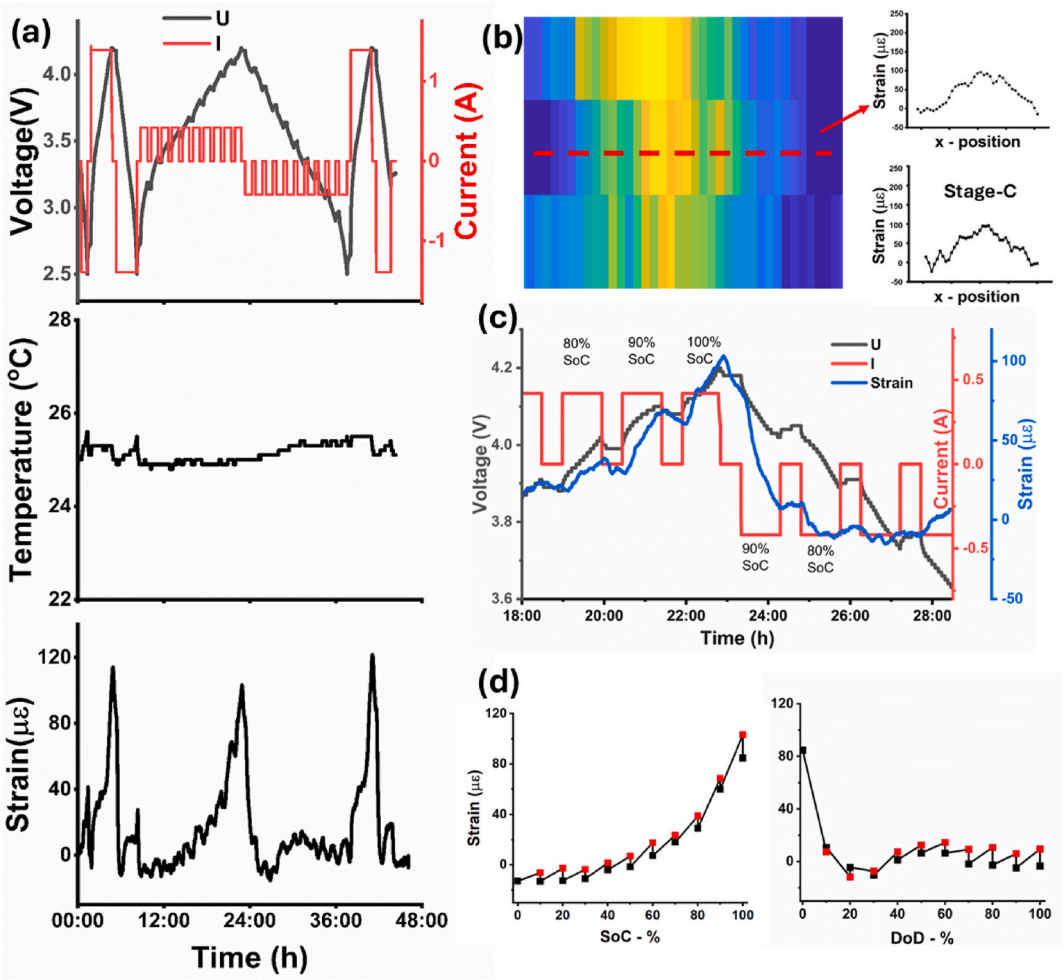

Fig. 4. Lithium intercalation/deintercalation induced battery swelling calibration. a. Top - Voltage and current under a SoC step test with C/10 rate, Middle – Minimised temperature variation during the SoC step test. Bottom – Measured strain profile. b. Battery swelling profile under a 100% SoC. The cross section of surface profile shows the identical pattern of the Stage C. c. Voltage and strain relaxation by withdrawing the applied charge/discharge current. d. Lithium intercalation induced strain versus state of charge – left and depth of discharge - right.

3.3. Analysis of battery swelling mechanisms

We can characterize the different swelling causes and observe three phases of battery swelling during the charge process and two phases during the discharge – black curve in Fig. 5(a and b). Under the phase C-1 (0%<SoC<20%), the strain is fast generated and accumulates to about 130με. In phase C-2 (20%<SoC<60%), there is a plateau where the battery reduces the swelling rate. The measured strain slowly rises to 150με. This plateau can be explained by the observed Li_XC_6 phase transition [31,49–51]. Graphite intercalation compounds undergo phase transitions through a sequence of dilute stage 1', stage 4, stage 3, stage 2 and final stage 1. The stage number is the graphite layers number without intercalated Lithium between two complete, crystalline intercalated lithium monolayers. The co-existence of stage 3, 2 and 1 at C-2 enables the moderate battery swelling during the constant speed of lithium movement. In phase C-3 (SoC>60%), the battery starts swelling fast to 232.1με till the end of CC charge. This is because stage 1 dominates lithium intercalation. Continuous intercalated lithium expands the fully crystalline graphite layers.

During the discharge phase D-1 (DoD<20%), the battery starts to shrink to the strain of 34.2με as previously indicated. In phase D-2 (DoD>20%), the battery reverses to swell until the end of discharge. The measured strain at the end of the discharge is 122.1με. Compared zero strain in the SoC-step result in Fig. 4(d), such increased strain generation is contributed by the temperature rise and applied C-rate. All these swelling spontaneously reduces to zero after electrical operation, and then the battery returns to its original status.

The proportion of battery swelling induced by various causes now can be quantified based on our proposed method and experiments. Thermal sensitivity is used to calculate the thermal induced swelling, which originates from the temperature variation (red zone). Lithium intercalation induced swelling is calculated as the strain generating under SoC step-test (blue zone). The remaining swelling is attributed to the applied C-rate (gray zone).

During the phase C-1, the temperature rises from 25.0°C to 26.4°C, and the thermal induced strain is calculated to be 35.7με. The lithium intercalation barely contributes to battery swelling during this stage. Because the graphite intercalation compounds mainly stay at dilute stage 1' and stage 4. The 1.5C rate induced swelling is fast generating and accumulating, together with the increasing temperature. The C-rate induced swelling takes up 64.7% of overall swelling at the end of C-1 phase. In phase C-2, the temperature stays stable, indicating the balance between the inside exothermic reaction and thermal dissipation. With the further increasing SoC in phase C-3, the lithium intercalation stage 1 contributes to the phase C-3 to accelerate the battery swelling. Although this phase transition does not generate additional heat, it enhances swelling from 92.1με to 122.9με.

At the end of CC charge (80% SoC), the thermal-induced strain is 38.6με, while the lithium intercalation induced strain is 31.9με. The C-rate induced strain is about 161.6με, accounting for 69.1% of the total

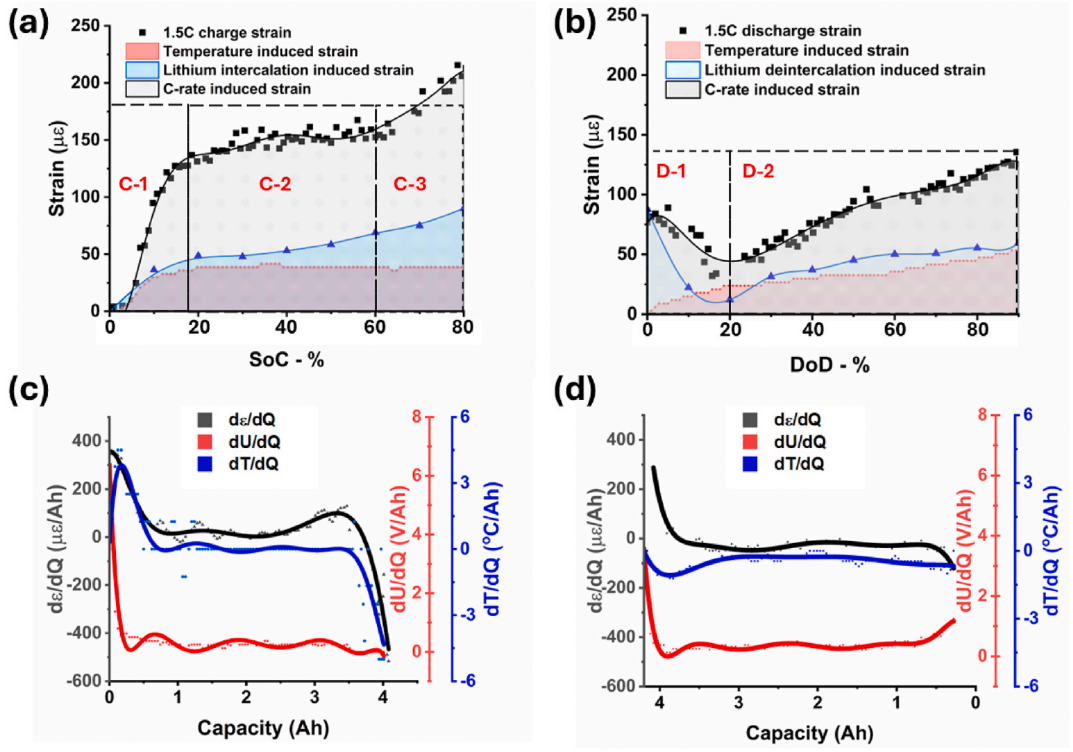

Fig. 5. Battery swelling causes characterisation. The contribution of thermal, lithium intercalation and applied C-rate to the battery swelling under a −1.5C CC charge, b - 1.5C CC discharge. The differential capacity analysis of strain, voltage and temperature under c −1.5C CC-CV charge, d- 1.5C CC discharge.

measured strain. At the end of CC discharge (90% DoD), the thermal-induced strain is 47.6με, while the lithium intercalation induced strain is 5.9με. The C-rate induced strain is 82.0με, about 60.5% of overall measured strain. All these indicate the dominate roll of C-rate induced strain in the fast cells operation.

Differential capacity analysis (DCA) is an effective method to characterize the battery process of phase transitions [20,52]. The DCA versus voltage-U, temperature-T and strain-ε under a 1.5C charge and discharge are presented in Fig. 5(c and d). The initial stage of charge (<10% SoC) undergoes significant phase change. Multiple parameters

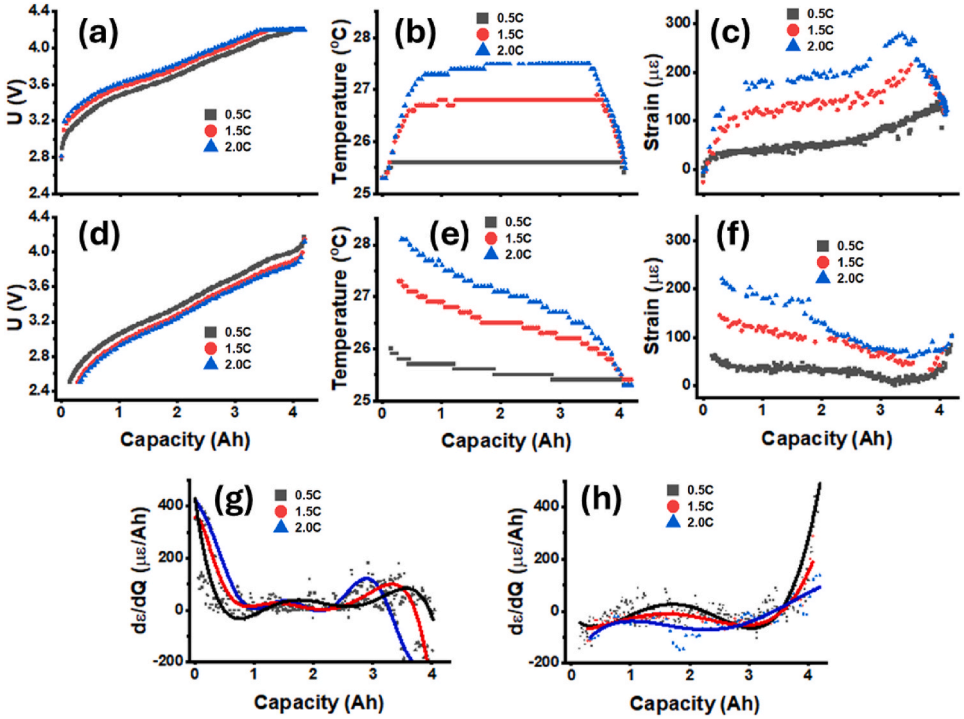

Fig. 6. Battery swelling characterisation based on various C-rate. The profile of voltage - a,d, temperature – b,e, strain -c,f and $d\varepsilon/dQ$-g,h under different applied C rates. a,b,c and g are with the charge process and d,e,f and h are with the discharge process.

peaks are observed and in a specific order. The voltage and strain start with peak at the start of charge. The temperature peak is the last and observed at 7.8% SoC. From the capacity of 17.8% SoC to 60% SoC, the voltage, strain and temperature experience a stable phase. With the further increasing beyond 60% SoC, the measured strain starts to rise as depicted in Fig. 5(a). After reaching 80% SoC, both temperature and strain decrease due to the dropping current in CV process. During the discharge, the voltage significantly drops with the first 3% DoD discharge. The strain reverses from shrinking to swelling at around 17% DoD, marking a switch point where the battery transitions from compression to expansion.

4. Discussion

4.1. Fast charge/discharge induced swelling

Previous studies of the thermal-induced, lithium intercalation-induced and C-rate induced swelling builds up the principle understanding of battery swelling composition. The battery swelling under various C-rate operation profiles is further characterized in the following.

The 0.5C,1.5C and 2.0C profiles of charge and discharge are carried out to further explore the swelling causes under various C-rates (Fig. 6). Spatial resolved optical measurement is shown in Supplementary1-Figs. S3–S5. During the charge process, the voltage gradually increases to 4.2V during a CC charge and then switched to CV charge at a capacity of 87.6% SoC, 78.0% SoC and 74.7% SoC under the rate of 0.5C, 1.5C and 2.0C, respectively. The increasing C-rates also leads to more heat generation. The maximum temperature is 25.6°C with 0.5C rate, while the maximum temperature is 27.5°C with 2.0C rate. During the CV process, the thermal rapidly dissipates with the reduced applied current. All mentioned strain phases of C-1, C-2 and C-3 are observed under different C-rates. The battery swelling is greatly enhanced by the increasing charge rate. The value of plateau in C-2 phase is around 50με under 0.5C rate and rises to 190με under 2.0C rate. The maximum strain at the end of CC charge is 137.9με and 278.1με at 0.5C and 2.0C rate, respectively. It is noted that, no matter the charge rates, the residual strain after the CV charge return to around 100με, proving the residual battery swelling at this stage is only related to the lithium intercalation.

As expected, higher discharge rate leads more heat generation. The maximum temperature at the end of 2.0C CC discharge is 28.1°C, compared to the 26.0°C under 0.5C discharge. Besides, the discharge process experiences a more active thermal generation-28.1°C than the charge process-27.5°C. The interesting part of D1- 'battery shrink' during the start of discharge happens at all C-rates. The battery surface returns to initial status under a 0.5C discharge D-1 phase. This result can be corresponding to SoC-step profile in Fig. 3. But under a 2.0C rate, the strain only reduces to 60.9με, indicating the less lithium deintercalation-induced shrink under higher discharge rate at D-1 stage. The other potential explanation is that the rapid generation of heat and applied high current both compromise the shrink of the battery. In the following phase D-2, the combined effect of thermal and high-rate operation pushes the strain to 220.3με at the end of 2.0 CC discharge, while the 0.5C discharge only generates 61.9με battery swelling.

Fast charge dominates the C-1 phase battery swelling and produces excessive heat. Such heat further enhances the battery swelling by causing mechanical expansion and accelerating electrochemical reaction. The $d\varepsilon/dQ$ during the C-2 plateau is barely affected by the fast charge. The temperature also stays constant in C-2 under various 0.5C, 1.5C and 2.0C rate, indicating equilibrium of the C-rate induced heat and heat disputation (e.g. 2.0C – 27.5°C, 0.5C-25.6°C). In C-3 phase, the charge rate impacts both the amplitude of $d\varepsilon/dQ$ and the corresponding capacity when the fastest strain generation. Under a 2.0C charge rate, the maximum value of $d\varepsilon/dQ$ is 121.4με/Ah at the capacity of 2.89Ah. While under a 0.5C charge rate, the maximum value of $d\varepsilon/dQ$ is 83.32με/Ah at the capacity of 3.35Ah.

During the D-1 phase, 0.5C discharge rate leads 439με/Ah of strain reduction, compared to the 87.2με/Ah with 2.0C rates, proving that the dominant factor for the battery shrink is the lithium deintercalation. Both the fast discharge and temperature rise are the reason of battery shrink compensation at this stage. These two factors both accelerate the surface swelling with the further discharge in D-2 phase.

4.2. Surface profile and proportion of swelling mechanism

Videos of operando battery surface profiles under 0.5C, 1.5C and 2.0C are provided in Supplementary2-4. Representative images are discussed in Fig. 7. The reported percentages for each swelling contribution are derived from a sequential analysis procedure involving OFDR calibration, temperature compensation, thermal calibration, and residual subtraction. Consequently, these values are subject to cumulative uncertainty from multiple sources and should be interpreted as approximate estimates rather than exact partitions of the total swelling response. This is particularly relevant under dynamic 1.5C operating conditions, where uncertainty propagation may be more pronounced.

During the slow charge/discharge process (0.5C), the charge process (Fig. 7(a,e)) induces greater strain than the discharge process (Fig. 7(b, f)), primarily due to lithium intercalation into the anode. The observed bump profile reflects a swelling gradient developing during charging, which highlights the underlying mechanisms of cell swelling, including non-uniform lithium intercalation, gas generation, and structural influences from the jellyroll and tab geometry.

Under high charge/discharge conditions (2.0C), more pronounced cell swelling occurs because of increased thermal activity and higher current density. The influence of lithium intercalation becomes less significant for the cell swelling, and both charge and discharge processes exhibit swelling at similar levels, suggesting the dominance of mechanical and thermal contributions to the overall expansion. Comparison across the three optical measurement regions—top, middle, and bottom—shows negligible variation along the battery width, confirming the reliability of the proposed optical fibre instrumentation. These results demonstrate that the swelling gradient primarily develops along the cell length rather than across its width.

The relative contributions of different swelling mechanisms are summarized in Fig. 7(i–l). At a 0.5C charge rate and 10% SoC, the applied C-rate accounts for most of the swelling (67.4%), followed by temperature-induced (18.6%) and lithium intercalation-induced swelling (13.9%). Near the end of the constant-current charging stage, the contributions from the C-rate and lithium intercalation become comparable (46.7% and 45.4%, respectively). When SoC reaches 100%, lithium intercalation dominates the swelling (92.7%) as the current ceases and the cell approaches ambient temperature equilibrium. In contrast, the temperature-induced swelling fraction decreases progressively from 18.6% at 10% SoC to 2.0% at 100% SoC. Under a 2.0C charge rate, temperature-induced swelling increases significantly, reaching 34.0% at 10% SoC, compared with 18.6% at 0.5C.

Throughout the entire 2.0C CC charge process (0–80% SoC), fast charging is the dominant source of swelling, contributing approximately 60% of the total expansion. The swelling composition remains stable below 50% SoC (C-rate: 60%; temperature: 30%; lithium intercalation: 10%). Above 80% SoC, lithium intercalation-induced swelling becomes the primary contributor to overall cell expansion.

During 0.5C discharge, the presence of the D-1 phase facilitates lithium deintercalation-induced contraction, reducing its contribution from 83.9% at 0% DoD to 1.2% at 20% DoD. Meanwhile, temperature-induced swelling gradually increases to 28.1% during constant-current discharge. At the end of discharge, lithium intercalation- and temperature-induced swelling contribute comparably (29.1% and 28.2%, respectively), while the discharge rate accounts for 42.7% of total swelling. Under the faster 2.0C discharge rate, a stable swelling regime appears for DoD >60%, where discharge rate–induced swelling accounts for approximately 55%, temperature effects for 35%, and

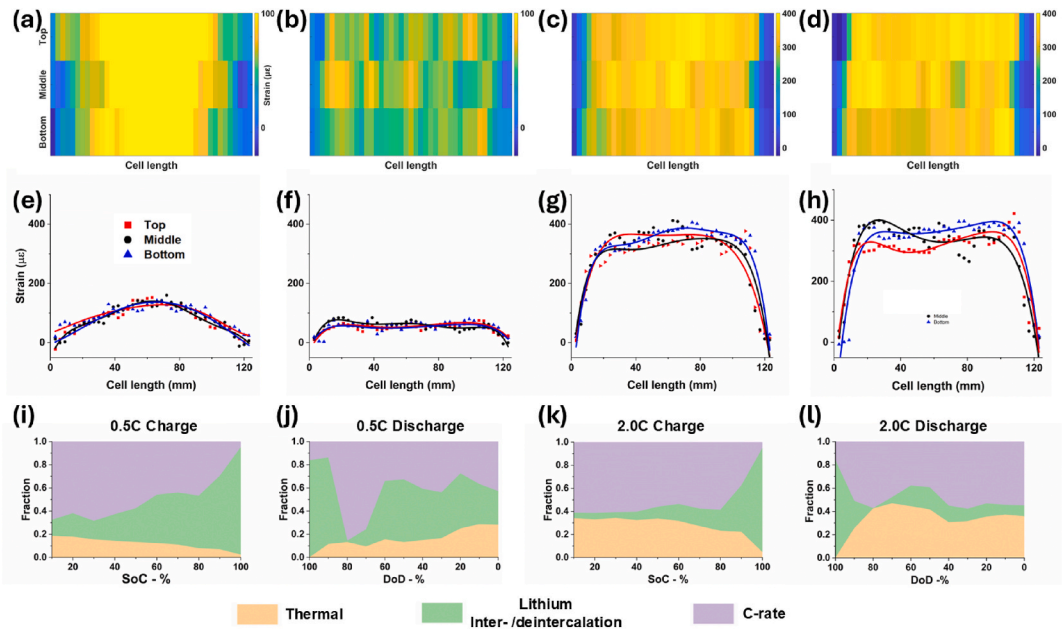

Fig. 7. Battery surface profile and proportion of swelling cause under different cell operation. Surface profile and corresponding optical measurement at cell top-middle-bottom segment - (a)(e) end of 0.5C CC charge, (b)(f) end of 0.5C CC discharge, (c)(g) end of 2.0C CC charge, (d)(h) end of 2.0C CC discharge. The proportion of swelling cause under different cell operation – (i) 0.5C CC-CV charge (j) 0.5C CC discharge (k) 2.0C CC-CV charge (l) 2.0C CC discharge.

lithium intercalation for about 10%. Although several observed features are consistent with mechanism-based interpretations, direct validation of the underlying electrode processes remains beyond the scope of the present work.

5. Conclusion

This paper explores the deep causes of battery swelling in multiparameter and multi-dimension by developing high resolution distributed optical sensor. The bump-like surface swelling indicates the concentrated deformation in the middle of pouch cells. And the shrink stage at the beginning of discharge reveals the lithium de-intercalation from the anode materials.

Revealed underlying swelling mechanisms open new direction for further battery investigation and optimization, such as 'hot spot' and 'weak point' monitoring of individual cells or pack. It expands the cell aging characterisation by introducing mechanical swelling into conventional electrical and thermal evaluation. This method is highly effective for various advancing the design and optimization of battery and energy applications. Extension of the proposed method to other cell formats, chemistries and pack-scale systems should be considered a promising direction for future work. The current results demonstrate the feasibility of the method for tracking short-term deformation behaviour. Its application to long-term aging, particularly to the quantification of irreversible swelling accumulated over cycling, also remains an important direction for future work. It can be investigated to adjust charge/discharge strategies for less battery deformation. The length of optical fibre can extend to hundreds or kilometres based on the OFDR demodulation, enable the further exploration of the EV battery pack or large containerised power storage for grid application.

CRediT authorship contribution statement

Zhen Guo: Conceptualization, Data curation, Formal analysis, Investigation, Methodology, Software, Validation, Visualization, Writing – original draft, Writing – review & editing. **Md Abul Kashem:** Formal analysis, Methodology, Software, Validation, Writing – review & editing. **Calum Briggs:** Investigation, Methodology, Resources, Writing – review & editing. **Lee Oldham:** Data curation, Methodology, Resources, Writing – review & editing. **Anup Barai:** Conceptualization, Funding acquisition, Investigation, Methodology, Project administration, Resources, Supervision, Writing – review & editing. **James Marco:** Conceptualization, Funding acquisition, Resources, Supervision, Writing – review & editing.

Declaration of competing interest

The authors declare that they have no known competing financial interests or personal relationships that could have appeared to influence the work reported in this paper.

Acknowledgements

The authors acknowledge the support of the Jaguar Land Rover Catapult (JLRC 9263). The authors would like to thank Harry Evans and Jason Page for project management.

Appendix A. Supplementary data

Supplementary data related to this article can be found online at https://doi.org/10.1016/j.jpowsour.2026.240296.

Data availability

Data will be made available on request.

References

[1] Yiding Li, Shicong Ding, Li Wang, Wenwei Wang, Cheng Lin, Xiangming He, On safety of swelled commercial lithium-ion batteries: a study on aging, swelling, and abuse tests, eTransportation (2024) 100368.
[2] Yuqing Chen, Yuqiong Kang, Yun Zhao, Li Wang, Jilei Liu, Yanxi Li, Zheng Liang, et al., A review of lithium-ion battery safety concerns: the issues, strategies, and testing standards, J. Energy Chem. 59 (2021) 83–99.
[3] A. Aufschläger, A. Durdel, A. Jossen, Identifying the origin of inhomogeneous degradation and irreversible swelling inside cylindrical 21700 high-energy lithium-ion cells, J. Energy Storage 90 (2024) 111726.
[4] Jeff R. Dahn, Tao Zheng, Yinghu Liu, J.S. Xue, Mechanisms for lithium insertion in carbonaceous materials, Science 270 (5236) (1995) 590–593.

[5] J.R. Dahn, Phase diagram of Li x C 6, Phys. Rev. B 44 (17) (1991) 9170.
[6] K.R. Kganyago, P.E. Ngoepe, Structural and electronic properties of lithium intercalated graphite LiC 6, Phys. Rev. B 68 (20) (2003) 205111.
[7] Hao Zhang, Yang Yang, Dongsheng Ren, Li Wang, Xiangming He, Graphite as anode materials: fundamental mechanism, recent progress and advances, Energy Storage Mater. 36 (2021) 147–170.
[8] Poornesh K. Koorata, Satyam Panchal, Roydon Fraser, Michael Fowler, Combined influence of concentration-dependent properties, local deformation and boundary confinement on the migration of Li-ions in low-expansion electrode particle during lithiation, J. Energy Storage 52 (2022) 104908.
[9] Kejie Zhao, Matt Pharr, Shengqiang Cai, Joost J. Vlassak, Zhigang Suo, Large plastic deformation in high-capacity lithium-ion batteries caused by charge and discharge, J. Am. Ceram. Soc. 94 (2011) s226–s235.
[10] Matt Pharr, Zhigang Suo, Joost J. Vlassak, Measurements of the fracture energy of lithiated silicon electrodes of Li-ion batteries, Nano Lett. 13 (11) (2013) 5570–5577.
[11] Kessel von, Otto, Arber Avdyli, Dragoljub Vrankovic, Kai Peter Birke, Swelling, pressure evolution and aging in high-silicon/graphite composite lithium-ion batteries, J. Power Sources 610 (2024) 234582.
[12] Tobias Deich, Mathias Storch, Kai Steiner, Andreas Bund, Effects of module stiffness and initial compression on lithium-ion cell aging, J. Power Sources 506 (2021) 230163.
[13] Zewen Zhang, Yuzhang Li, Rong Xu, Weijiang Zhou, Yanbin Li, Solomon T. Oyakhire, Yecun Wu, et al., Capturing the swelling of solid-electrolyte interphase in lithium metal batteries, Science 375 (6576) (2022) 66–70.
[14] Rochelle Weber, Matthew Genovese, A.J. Louli, Samuel Hames, Cameron Martin, Ian G. Hill, J.R. Dahn, Long cycle life and dendrite-free lithium morphology in anode-free lithium pouch cells enabled by a dual-salt liquid electrolyte, Nat. Energy 4 (8) (2019) 683–689.
[15] Kang Xu, Electrolytes and interphases in Li-ion batteries and beyond, Chem. Rev. 114 (23) (2014) 11503–11618.
[16] Qianqian Liu, Chunyu Du, Bin Shen, Pengjian Zuo, Xinqun Cheng, Yulin Ma, Geping Yin, Yunzhi Gao, Understanding undesirable anode lithium plating issues in lithium-ion batteries, RSC Adv. 6 (91) (2016) 88683–88700.
[17] Mathias Petzl, Michael Kasper, Michael A. Danzer, Lithium plating in a commercial lithium-ion battery–A low-temperature aging study, J. Power Sources 275 (2015) 799–807.
[18] Weiyang Li, Hongbin Yao, Kai Yan, Guangyuan Zheng, Zheng Liang, Yet-Ming Chiang, Yi Cui, The synergetic effect of lithium polysulfide and lithium nitrate to prevent lithium dendrite growth, Nat. Commun. 6 (1) (2015) 7436.
[19] Ben Rowden, Nuria Garcia-Araez, A review of gas evolution in lithium ion batteries, Energy Rep. 6 (2020) 10–18.
[20] Jessica Hemmerling, Johannes Schäfer, Tobias Jung, Tina Kreher, Marco Ströbel, Carola Gassmann, Jonas Günther, Alexander Fill, Kai Peter Birke, Investigation of internal gas pressure and internal temperature of cylindrical Li-ion cells to study thermodynamical and mechanical properties of hard case battery cells, J. Energy Storage 59 (2023) 106444.
[21] Weihe Kong, Hong Li, Xuejie Huang, Liquan Chen, Gas evolution behaviors for several cathode materials in lithium-ion batteries, J. Power Sources 142 (1–2) (2005) 285–291.
[22] Bernhard Rieger, Steffen Schlueter, Simon V. Erhard, Johannes Schmalz, Gunther Reinhart, Andreas Jossen, Multi-scale investigation of thickness changes in a commercial pouch type lithium-ion battery, J. Energy Storage 6 (2016) 213–221.
[23] Ki-Yong Oh, Bogdan I. Epureanu, A novel thermal swelling model for a rechargeable lithium-ion battery cell, J. Power Sources 303 (2016) 86–96.
[24] Daniel Sauerteig, Svetlozar Ivanov, Holger Reinshagen, Andreas Bund, Reversible and irreversible dilation of lithium-ion battery electrodes investigated by in-situ dilatometry, J. Power Sources 342 (2017) 939–946.
[25] Leilei Wang, Woohyuk Choi, Kisoo Yoo, Kanghyun Nam, Tae Jo Ko, Jungwook Choi, Stretchable carbon nanotube dilatometer for in situ swelling detection of lithium-ion batteries, ACS Appl. Energy Mater. 3 (4) (2020) 3637–3644.
[26] P. Blazek, P. Westenberger, S. Erker, A. Brinek, T. Zikmund, D. Rettenwander, N. P. Wagner, J. Keckes, J. Kaiser, T. Kazda, P. Vyroubal, Axially and radially inhomogeneous swelling in commercial 18650 Li-ion battery cells, J. Energy Storage 52 (2022) 104563.
[27] Chengcheng Chen, Yong Wei, Zhenbo Zhao, Yabing Zou, Daojun Luo, Investigation of the swelling failure of lithium-ion battery packs at low temperatures using 2D/3D X-ray computed tomography, Electrochim. Acta 305 (2019) 65–71.
[28] Emanuele Michelini, Patrick Höschele, Simon Franz Heindl, Simon Erker, Christian Ellersdorfer, Experimental investigation on reversible swelling mechanisms of lithium-ion batteries under a varying preload force, Batteries 9 (4) (2023) 218.
[29] Lisa K. Willenberg, Philipp Dechent, Georg Fuchs, Dirk Uwe Sauer, Egbert Figgemeier, High-precision monitoring of volume change of commercial lithium-ion batteries by using strain gauges, Sustainability 12 (2) (2020) 557.
[30] P.K. Leung, C. Moreno, Iain Masters, Sumit Hazra, B. Conde, M.R. Mohamed, R. J. Dashwood, Bhagat Rohit, Real-time displacement and strain mappings of lithium-ion batteries using three-dimensional digital image correlation, J. Power Sources 271 (2014) 82–86.
[31] Begum Gulsoy, Timothy A. Vincent, Calum Briggs, Jonathan EH. Sansom, James Marco, In-situ measurement of internal gas pressure within cylindrical lithium-ion cells, J. Power Sources 570 (2023) 233064.
[32] O. Yu Egorkina, A.M. Skundin, The effect of temperature on lithium intercalation into carbon materials, J. Solid State Electrochem. 2 (1998) 216–220.
[33] Elna JK. Nilsson, Annika Ahlberg Tidblad, Gas emissions from lithium-ion batteries: a review of experimental results and methodologies, Batteries 10 (12) (2024) 443.
[34] Bin Xu, Weiping Diao, Guangrui Wen, Song-Yul Choe, Jonghoon Kim, Michael Pecht, Decoupling the thermal and non-thermal effects of discharge C-rate on the capacity fade of lithium-ion batteries, J. Power Sources 510 (2021) 230390.
[35] Ti Dong, Peng Peng, Fangming Jiang, Numerical modeling and analysis of the thermal behavior of NCM lithium-ion batteries subjected to very high C-rate discharge/charge operations, Int. J. Heat Mass Tran. 117 (2018) 261–272.
[36] Gaoce Han, Jize Yan, Zhen Guo, David Greenwood, James Marco, Yifei Yu, A review on various optical fibre sensing methods for batteries, Renew. Sustain. Energy Rev. 150 (2021) 111514.
[37] Albero Blanquer, Florencia Marchini Laura, Jan Roman Seitz, Nour Daher, Fanny Bétermier, Jiaqiang Huang, Charlotte Gervillié, Jean-Marie Tarascon, Optical sensors for operando stress monitoring in lithium-based batteries containing solid-state or liquid electrolytes, Nat. Commun. 13 (1) (2022) 1153.
[38] Yanpeng Li, Yi Zhang, Zhen Li, Zhijun Yan, Xiangpeng Xiao, Xueting Liu, Jie Chen, Yue Shen, Qizhen Sun, Yunhui Huang, Operando decoding of surface strain in anode-free lithium metal batteries via optical fiber sensor, Adv. Sci. 9 (26) (2022) 2203247.
[39] Weihan Wang, Yanyun Zhang, Bin Xie, Lang Huang, Shanmu Dong, Gaojie Xu, Guanglei Cui, Deciphering advanced sensors for life and safety monitoring of lithium batteries, Adv. Energy Mater. (2024) 2304173.
[40] Zhenyang Ding, Chenhuan Wang, Kun Liu, Junfeng Jiang, Di Yang, Guanyi Pan, Zelin Pu, Tiegen Liu, Distributed optical fiber sensors based on optical frequency domain reflectometry: a review, Sensors 18 (4) (2018) 1072.
[41] Zhen Guo, Gaoce Han, Jize Yan, David Greenwood, James Marco, Yifei Yu, Ultimate spatial resolution realisation in optical frequency domain reflectometry with equal frequency resampling, Sensors 21 (14) (2021) 4632.
[42] Zhen Guo, Jize Yan, Gaoce Han, Yifei Yu, David Greenwood, James Marco, High-resolution ϕ-OFDR using phase unwrap and nonlinearity suppression, J. Lightwave Technol. 41 (9) (2023) 2885–2891.
[43] Zhen Guo, Calum Briggs, Timothy A. Vincent, Begum Gulsoy, Jonathan EH. Sansom, James Marco, Global thermal image of cylindrical 21700 Li-ion batteries with distributed optical fibre sensor, J. Power Sources 592 (2024) 233980.
[44] Ki-Yong Oh, Jason B. Siegel, Lynn Secondo, Sun Ung Kim, Nassim A. Samad, Jiawei Qin, Dyche Anderson, et al., Rate dependence of swelling in lithium-ion cells, J. Power Sources 267 (2014) 197–202.
[45] Ki-Yong Oh, Bogdan I. Epureanu, A novel thermal swelling model for a rechargeable lithium-ion battery cell, J. Power Sources 303 (2016) 86–96.
[46] Gerardine G. Botte, Bradley A. Johnson, Ralph E. White, Influence of some design variables on the thermal behavior of a lithium-ion cell, J. Electrochem. Soc. 146 (3) (1999) 914.
[47] Li Song, James W. Evans, Electrochemical-thermal model of lithium polymer batteries, J. Electrochem. Soc. 147 (6) (2000) 2086.
[48] Atsushi Funabiki, Minoru Inaba, Takeshi Abe, Zempachi Ogumi, Stage transformation of lithium-graphite intercalation compounds caused by electrochemical lithium intercalation, J. Electrochem. Soc. 146 (7) (1999) 2443.
[49] Yinsheng Guo, Raymond B. Smith, Zhonghua Yu, Dmitri K. Efetov, Junpu Wang, Philip Kim, Martin Z. Bazant, Louis E. Brus, Li intercalation into graphite: direct optical imaging and Cahn–Hilliard reaction dynamics, J. Phys. Chem. Lett. 7 (11) (2016) 2151–2156.
[50] K.R. Kganyago, P.E. Ngoepe, Structural and electronic properties of lithium intercalated graphite LiC 6, Phys. Rev. B 68 (20) (2003) 205111.
[51] Kristin Persson, Vijay A. Sethuraman, Laurence J. Hardwick, Yoyo Hinuma, Ying Shirley Meng, Anton Van Der Ven, Venkat Srinivasan, Robert Kostecki, Gerbrand Ceder, Lithium diffusion in graphitic carbon, J. Phys. Chem. Lett. 1 (8) (2010) 1176–1180.
[52] Lucca Matuck, João P. Santos, Fábio Freitas, Luís B. Fontes, Jörg Bierlich, Sylvie Geniès, João L. Pinto, Marta S. Ferreira, Olivier Raccurt, Micael Nascimento, Towards smart and secure batteries: linking pressure and temperature profiles with electrochemical behavior through hybrid optical fiber sensors, Chem. Eng. J. (2024) 156806.